Journal of Colloid and Interface Science 590 (2021) 446–457

Contents lists available at ScienceDirect

Journal of Colloid and Interface Science

journal homepage: www.elsevier.com/locate/jcis

Regular Article

# A pore network modelling approach to investigate the interplay between local and Darcy viscosities during the flow of shear-thinning fluids in porous media

Antonio Rodríguez de Castro [a,*], Benoit Goyeau [b]

[a] Arts et Metiers Institute of Technology, MSMP, HESAM Université, F-51006 Châlons-en-Champagne, France
[b] Laboratoire EM2C, UPR CNRS 288, Centrale-Supélec, Université Paris-Saclay, 3 rue Joliot-Curie, 91190 Gif-sur-Yvette, France

## GRAPHICAL ABSTRACT

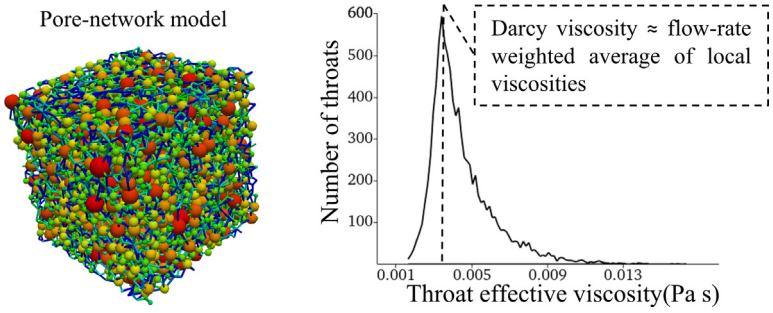


## ARTICLE INFO

*Article history:*
Received 8 December 2020
Revised 14 January 2021
Accepted 25 January 2021
Available online 2 February 2021

*Keywords:*
Shear-thinning fluids
Pore network modelling
Upscaling method
Shear-viscosity distribution
Hydraulic tortuosity
Solid-fluid interactions

## ABSTRACT

During the flow of non-Newtonian fluids in porous media, the relationships between macroscopic quantities are governed by extremely complex microscopic fluid dynamics resulting from solid-fluid interactions. Consequently, the Darcy-scale viscosity exhibited by a shear-thinning fluid depends on the injection velocity, contrarily to the case of Newtonian fluids. In the present work, pore network modelling is used to investigate the relationships between local and macroscopic viscosities during the flow of shear-thinning fluids in 3D porous media. Special efforts are devoted to 1) identifying the influence of the viscosity exhibited by the fluid within the constrictions of the preferential flow paths on the value of Darcy-scale viscosity and 2) proposing an analytical expression to upscale viscosity from the local viscosity values. To go further, the reduction in average hydraulic tortuosity stemming from the directional nature of shear-thinning behavior in 3D porous media will also be quantified. The results of the present study show that Darcy-scale viscosity can be accurately calculated as the flow-rate weighted average of local viscosities in the investigated media. Moreover, the velocity maps provided by the proposed pore network flow simulations are suitable to assess hydraulic tortuosity reduction as compared to the flow of a Newtonian fluid.

© 2021 Elsevier Inc. All rights reserved.

## 1. Introduction

Shear-thinning fluids are ubiquitous in environmental, industrial and biological environments. These fluids are mixtures in which two phases coexist, and they are therefore structured to

* Corresponding author at: Arts et Métiers ParisTech, Rue Saint-Dominique, 51006 Châlons-en-Champagne, France.
*E-mail address:* antonio.rodriguezdecastro@ensam.eu (A. Rodríguez de Castro).

https://doi.org/10.1016/j.jcis.2021.01.081
0021-9797/© 2021 Elsevier Inc. All rights reserved.

varying extents. When a continuum and homogeneous description is assumed, shear-thinning fluids are mainly characterised by a space-averaged viscosity which is dependent on the value of the applied shear-rate. Such dependence is explained by the variations in the dispersion of the structural units due to increased orientation, stretching deformation or disintegration when shear rate is increased [1]. Some examples of shear-thinning fluids are paints, blood, ketchup, foams and polymer solutions.

Numerous important industrial applications involve the injection of shear-thinning fluids through porous media [2]. For example, polymers such as xanthan gum and synthetic polyacrylamide in its partially hydrolyzed form (HPAM) are usually added to aqueous solutions to improve the macroscopic sweep efficiency in soil remediation operations [3–5]. This is achieved due to the improvement in the viscosity ratio between the injected and displaced fluids provided by these additives. Apart from underground operations, understanding the circulation of blood and interstitial fluid (which are shear-thinning fluids) through the pores of bone tissue during transport of nutrients to the bone cells and evacuation of waste is also expected to shed light on several biomedical problems [6,7].

Injecting a complex fluid through a porous medium generates a wide diversity of local viscosities. In particular, the variability in terms of morphology, topology and characteristic lengths of the pores severely affects the distribution of local viscosities and velocities [2]. Therefore, the local interactions between the fluid and the medium microstructure govern the pressure losses throughout the medium and affect macroscopic flow. For most situations, Darcy viscosity can only be related to local viscosities by using empirical shift factors [4,5,8]. However, the shift factors approach fails to provide reliable relationships between local and macroscopic viscosities for shear-thinning fluids exhibiting Newtonian plateau viscosities at the very low and very high shear rates [9,10], which restricts the interest of this method mainly to the case of simple power-law fluids. Without using any shift factor, Eberhard et al. [11] derived a semi-analytical expression for the local viscosity profile of a Carreau fluid. Their approach required estimating a unique characteristic capillary radius for a given porous medium. Then, the velocity and shear rates profiles were determined in such a capillary and the Darcy viscosity was estimated by averaging the viscosity profile over the cross section. For a pack of equal spheres, the authors defined the characteristic radius as being the maximal radius of the void space between three beads that are in contact with each other. This model was experimentally validated only within the transition region close to the low-shear-rates viscosity plateau with some reservations imposed by the high uncertainty of the low-shear-rate measurements.

The preceding methods do not provide the distribution of viscosities within the pores space. In contrast, numerical simulations could potentially be used to achieve this goal. In this regard, Morais et al. [12] performed pioneer Direct Numerical Simulations (DNS) of the flow of shear-thinning fluids, with and without yield stress, through small samples of a 3D porous medium of extremely high porosity generated by a Swiss-Cheese model. The results of the preceding work showed that the interactions between the disordered microstructure, the fluid rheological properties, and the inertial effects accounted for the enhancement of the macroscopic hydraulic conductance at intermediate values of Reynolds number. However, neither local viscosity distributions nor the tortuosity of the streamlines were characterized. DNS were also used in the past to show that shear-thinning fluids exhibit high values of local viscosity in the microscopic conduits of the porous media in which the pressure gradient is low, which results in flow being diverted from these zones. This is the case of the pore channels that are oriented nearly perpendicularly to the main flow direction On this topic, previous research works showed that the average macroscopic tortuosity of flow paths was lower during flow of shear-thinning and yield stress fluids as compared to the flow of a Newtonian fluids, both in rough-walled fractures [13] and 2D porous with varying levels of microstructural disorder media [14]. However, the conclusions of these works have not yet been extended to the case of 3D porous media, which is mainly due to the demanding requirements in terms of computational resources to perform DNS for the flow of complex fluids.

Sochi [15] reviewed the four main approaches for describing the flow of non-Newtonian fluids through porous media: continuum models, bundle of tubes models, numerical methods, and pore-scale network modeling. This author concluded that, despite being unable to account for all microstructural complexities, pore network modeling is the most efficient choice. Indeed, pore network approach provides accurate predictions of experimental measurements in many important applications [15,16], including blood flow in arteries and tissues, food processing and environmental engineering. The advantage of using pore network models in flow simulations is double. First, the demanding computational cost of DNS are drastically reduced, which is particularly important in the presence of non-linearities as those arising from shear-thinning behavior. Moreover, the use of regular pore shapes for which the local viscosity can be analytically expressed as a function of the pressure gradient allows for the definition of an equivalent viscosity in each pore.

López et al. [9] extracted pore networks from artificially generated 3D images of sand packs and sandstones and proposed a flow model to predict Darcy-scale viscosity for the flow of truncated power-law fluids. Their predictions did not involve the use of any adjustable parameter and proved to be accurate within the power-law region when compared with experiments. Nevertheless, divergences between predictions and experiments were observed in the range of Darcy viscosities close to the Newtonian viscosity plateaus, which was potentially due to the inability of the truncated power-law model to represent the bulk rheology of real shear-thinning fluids in the corresponding range of shear rates. A similar approach was used by Sochi and Blunt [17] and Sochi [18] to incorporate the effects of yield stress in the pore network flow simulations, leading to variable agreement between numerical and experimental results. Such variable agreement was expected to be improved by considering particle adsorption on the pore walls and other neglected effects. As an alternative to typical capillary tube networks, Balhoff and Thompson [19] performed pore network flow simulations of Ellis and power-law fluids through packs of spheres using the original geometry of pore throats and obtained satisfactory agreement with experiments. In their method, approximate expressions were needed for the flow through the real throat geometries, which were obtained by performing DNS. Furthermore, single and multiphase flows of shear-thinning fluids in 2D pore networks consisting of regular geometries were numerically simulated by Tsakiroglou [20,21]. The author reported good agreement in many configurations between the predictions of capillary pressure curves, relative permeability and Darcy velocity vs. pressure gradient relationships and the experimental measurements. Other authors also obtained good agreement between Darcy viscosity predicted from 2D [22] and 3D pore network flow simulations [23] and the experimentally measured values. Nevertheless, neither in this case were the distributions of local shear viscosities and their relationship with Darcy viscosity addressed. It was only recently that Eberhard et al. [24] presented an experimental method to obtain the spatial distribution of local viscosities of non-Newtonian fluids within the pores in micromodels. This was achieved by using high resolution image velocimetry to map local shear rates, and the results showed that the injection-velocity dependent variability of local viscosities affects flow channelization and transport processes.

Modelling the relationships between pore-scale flow and macroscale quantities is required to closely simulate the movement of complex fluids at larger scales. However, to the best knowledge of the authors, the value of Darcy-scale viscosity has not been upscaled from the distribution of local viscosities throughout the whole pore network of a 3D porous medium in any previous literature work. Motivated by this gap, the purpose of the current work is to develop a method for predicting the value of the macroscopic apparent viscosity from the distribution of local viscosities during flow in unconsolidated porous media. With this objective in mind, pore network flow simulations are presented in which shear-thinning fluids with realistic rheological behavior are injected through different pore networks extracted from artificial and natural porous samples. The computed distributions of microscopic flow rates and the extracted pore characteristic lengths will be used to compute the viscosities in the pore conduits. Then, a weighted average expression allowing for viscosity upscaling will be deduced and validated from the comparison of the obtained distributions of local viscosities to the macroscopic viscosity values. Furthermore, the dependence of tortuosity on the injection velocity will be numerically investigated for the first time during the flow of complex fluids in 3D unconsolidated media, by using the velocity maps provided by the pore network flow simulations as input.

## 2. Theoretical considerations: bulk, effective and Darcy viscosities.

The dependence of shear viscosity on shear rate during steady simple shear flow of shear-thinning fluids, including semi-dilute polymer solutions and biologic fluids, is frequently represented by the empirical Carreau model [25]:

$$\frac{\mu-\mu_\infty}{\mu_0-\mu_\infty}=\left[1+(\lambda\dot{\gamma})^2\right]^{\frac{n-1}{2}} \tag{1}$$

In this expression, $\mu$ is the shear viscosity, $\dot{\gamma}$ is the shear rate, $\lambda$ is the longest relaxation time, n is the flow index, $\mu_0$ is the low shear rate Newtonian viscosity plateau value and $\mu_\infty$ is the high shear rate Newtonian viscosity plateau value, with $\mu_\infty$ being very close to the viscosity of the solvent in most cases [3]. In the case of polymer solutions, the values of $\mu_0$, $\lambda$ and n mainly depend on the polymer concentration $C_p$, and such shear-thinning behaviour stems from the alignment and concentration of the polymer macromolecules in the solution. Indeed, higher shear rates result in the macromolecules being more properly aligned with the direction of flow, which reduces the drag between fluid layers and, and consequently the viscosity exhibited by the polymer solution. Contrarily to the simple power-law model, Carreau's equation reliably represents the transitions from the intermediate shear rates region with shear-thinning behavior to the low shear rate and high shear rate Newtonian viscosity plateaus, which are observed both during the rheometric measurements of the bulk rheology and during flow in porous media [8]. Moreover, Carreau's model is based on molecular network theory and has a firm theoretical basis [26].

The truncated power-law model has also been widely used in the literature [9,13,23], which is expressed as:

$$\mu=\mathrm{Max}\left[\mu_{T,\infty};\mathrm{Min}\left(c_T\dot{\gamma}^{n_T-1};\mu_{T,0}\right)\right] \tag{2}$$

where $\mu_{T,0}$ and $\mu_{T,\infty}$ are the low shear rates and high shear rates viscosity plateaus, $c_T$ is the consistency and $n_T$ is the shear-thinning index. This model allows for the development of simple analytical solutions to relate effective viscosity to pressure drop during the flow of a non-Newtonian fluid in a capillary, which is not the case of Carreau fluids despite recent progress [11,15,27,28]. Nonetheless, whereas the truncated power law approximates reasonably well Carreau model under low shear rates, the differences are important at the highest shear rates [3].

From Eq. (1), it can be deduced that in the region far from the low shear viscosity plateau, i.e., when $\dot{\gamma}\gg\frac{1}{\lambda}$, Carreau's law can be expressed as follows [3,29]:

$$\mu\approx\mu_\infty+(\mu_0-\mu_\infty)\lambda^{n-1}\dot{\gamma}^{n-1}=\mu_\infty+c\dot{\gamma}^{n-1} \tag{3}$$

To take into account the viscosity plateau at the lowest shear-rates, Eq. (3) can be modified as:

$$\mu=\mathrm{Min}(\mu_0;\mu_\infty+c\dot{\gamma}^{n-1}) \tag{4}$$

This simplified version of Carreau model can be efficiently implemented in the pore network simulations, as will be explained in subsection 3.3.

As mentioned above, no analytical expression relating the flow rate or pressure gradient to the effective viscosity during the flow of a Carreau fluid through a cylindrical capillary is available. Consequently, the following empirical expression will be considered to approximate the effective viscosity of the fluids exhibiting the dynamic bulk viscosity given by simplified Carreau model (Eq. (4)):

$$\mu_{eff}=\mathrm{Min}\left(\mu_0,\mu_\infty+c\left(\frac{3n+1}{4n}\right)\left(\frac{r\Delta P}{2cL}\right)^{\frac{n-1}{n}}\right) \tag{5}$$

Eq.(5) is obtained by introducing the effective shear rate exhibited by a power-law fluid during its flow through a cylinder $\dot{\gamma}_{power-law}=c\left(\frac{3n+1}{4n}\right)\left(\frac{r\Delta P}{2cL}\right)^{\frac{1}{n}}$ in Eq.(4). It may be noted that the previous equation reduces to the exact analytical expression of $\mu_{eff}$ for power-law fluid flow through a cylindrical capillary when $\mu_\infty$ = 0 and $\mu_0\to\infty$. This expression also ensures that the Newtonian viscosity plateaus are attained at the lowest and highest shear rates. Similar empirical approximations of $\mu_{eff}$ were also used in the works of López [3], Perrin et al. [22] and Shende et al. [28]. In order to assess the accuracy of the approximations of $\mu_{eff}$ provided by Eq. (5), these were compared to the results of direct numerical simulations of the creeping flow of fluids with different values of c and n through a cylindrical capillary. The average and maximum errors were close to 7% and 12%, respectively, for all the rheological parameters tested in the simulations over four orders of magnitude of the imposed pressure gradient. Therefore, Eq. (5) will be used in subsection 3.3. to calculate the effective viscosity value in each cylindrical conduit of the pore networks.

For the single-phase creeping flow of incompressible fluids through a porous medium at the macroscopic scale, Darcy viscosity $\mu_D$, also known as apparent viscosity, can be calculated from Darcy's law as:

$$\mu_D=-\frac{KA}{Q}\nabla P \tag{6}$$

with K being the intrinsic permeability of the porous medium, A being its cross-sectional area, Q being the injection flow rate and $\nabla P$ being the pression gradient.

## 3. Numerical simulations

### 3.1. Investigated porous media and fluids

The freely available digital 3D image of a pack of identical spheres obtained by Finney [30,31] was considered in the current analysis. The pack of spheres used by the latter author was generated by shaking together monodisperse 1/4-in-diameter steel ball-bearings, and the 3D image was optically obtained using a special marking technique. Discretization of the digital image was performed using cubic voxels of 0.04 length (in units normalized by

sphere radius). The total size of the image was 500 × 500 × 500 voxels. The same image was scaled to each of the sphere diameters $d_s$ considered in this work (1 mm, 3 mm, 4 mm and 5 mm) using ImageJ software. Moreover, a poorly sorted unconsolidated fluvial sand pack from southern Australia was also investigated. This medium was imaged using an X-ray micro-CT device by Sheppard and Prodanovic [32] and is also freely available. The 3D image of the sand pack is displayed in Fig. 1(a). The voxel size was 9.184 μm and the total size of the image was 512 × 512 × 512 voxels.

In order to reproduce realistic conditions in the current numerical experiments, the rheological parameters of the three investigated shear-thinning fluids, listed in Table 1, were chosen to be equal to those used in the experimental work presented by Rodríguez de Castro and Radilla [33]. These authors injected three different xanthan gum solutions through a set of 4 packs of spherical beads. The shear-rheology of these polymer solutions was shown to be well represented by the rheological model expressed by Eq. (4). Given that $\mu_0$ was not characterized by the preceding authors, a value of $\mu_0$ = 100 Pa s were used in the present numerical simulations. As can be deduced from Table 1, an increase in the polymer concentration $C_p$ leads to a more pronounced shear-thinning behaviour (lower values of n) and highest values of the consistency. In the context of biomedical applications, xanthan gum solutions have been traditionally used in the literature as blood analog fluids [34,35].

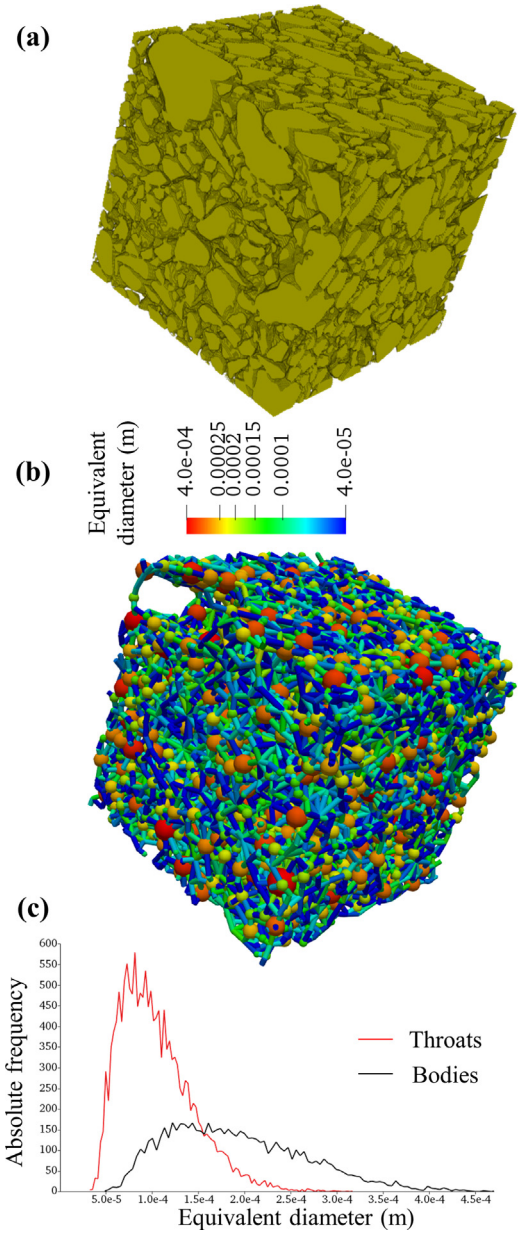


**Fig. 1.** Pore network model of the investigated sand pack. (a) Input 3D image of the sand pack for the extraction of the pore network [32]. (b) Image of the network as extracted from the 3D digital image. Warmer colors correspond to greater equivalent diameters of the pore bodies and pore throats. (c) Body size distribution and throat size distribution of the conducting throats.

The Carreau model parameters for a given fluid can be obtained by following the experimental procedures described in the literature [29,33]. In these previous works, a stress-controlled rheometer equipped with a cone-and-plate geometry was used. The applied shear stresses were linearly sampled from 0 to a maximum value producing a shear rate of approximately 1000 $s^{-1}$. Then, a least squares method was used to fit the shear stress vs. shear rate experimental data to Carreau's model (Eq. (1)).

### 3.2. Pore network extraction

Pore network modeling allows for the reduction of the computational resources required for the simulation of flow in porous media at the pore scale as compared to direct numerical simulations while ensuring reasonable accuracy [36]. The digital images of the packs of spherical beads and the sand pack presented in the preceding subsection were used as input for the extraction of equivalent pore networks consisting of spherical pore bodies connected by cylindrical throats. In the procedure followed to extract such a simplified geometry, the subnetwork of the oversegmented watershed (SNOW) algorithm presented by Gostick [37] was used. SNOW algorithm starts by extracting the distance map of the void spaces, which is subsequently filtered through the exclusion of the peaks on saddles and plateaus. Next, the peaks that lie very near each other are merged, thus generating a set of markers. These markers are used as inputs to a marker-based watershed algorithm that finds the basins of the distance map, yielding the segmentation of each pore region. SNOW algorithm is included in PoreSpy [38], an open-source toolkit for quantitative post-processing of porous media digital images. By using the preceding procedure, the pore networks displayed in Fig. 1(b) and Figure 2(a)were obtained from the digital images. In the case of the pack of spherical beads, the pore networks corresponding to different sphere diameters (1 mm, 3 mm, 4 mm and 5 mm) were also extracted. Then, the porosities of both types of porous media, their permeabilities, their tortuosity values and some essential features of their microstructure were computed from the extracted pore networks. These characteristics are listed in Table 2 together with the dimensions of the analyzed samples. It should be noted that the body and throat dimensions listed in this table are given in terms of the equivalent diameters. The equivalent diameter of a pore body is equal to the diameter of a sphere with same volume as the pore, while the equivalent diameter of a throat is equal to the diameter of a circle with same area as the throat. The distributions of body equivalent diameters and throat equivalent diameters are represented in Fig. 1(c) for the sand pack and in Fig. 2(c) for the pack of 4 mm spheres. The maxima shown in the Fig. 1(c) and the Fig. 2(c) represent the modal classes of the throat and body sizes.

### 3.3. Flow simulations

It must be mentioned that establishing relationships between the local viscosities at the pore scale and the efficient viscosity at the Darcy scale is not straightforward in the presence of microstructural heterogeneity. Indeed, Darcy-scale viscosity

**Table 1**
Shear-rheology parameters of the investigated fluids, which correspond to those of the xanthan gum solutions used by Rodríguez de Castro and Radilla [33] in their laboratory experiments. Given that $\mu_0$ was not characterized by the preceding authors, a value of $\mu_0$ = 100 Pa s was used in the present numerical simulations.

| Fluid | c(Pa.s$^n$) | n | $\mu_\infty$(Pa.s) | $\mu_0$(Pa.s) |
|---|---|---|---|---|
| 200 ppm xanthan gum solution | 0.0048 | 0.66 | 0.0011 | 100 |
| 500 ppm xanthan gum solution | 0.024 | 0.58 | | |
| 700 ppm xanthan gum solution | 0.042 | 0.52 | | |

**Table 2**
Dimensions, porosities, permeabilities, tortuosities and essential microstructural features of the investigated pore networks. 500 ppm at the highest u (50000 Pa pour sand pack).

| Sample | Pack of spheres (4 mm) | Sand pack |
|---|---|---|
| Dimensions [mm] | 40 × 40 × 40 | 4.70 × 4.70 × 4.70 |
| ε [–] | 0.36 | 0.36 |
| K [m$^2$] | 7.07 × 10$^{-9}$ | 4.97 × 10$^{-11}$ |
| $T_N$ [–] | 1.55 | 1.59 |
| Mean body diameter [m] | 1.93 × 10$^{-3}$ | 1.73 × 10$^{-4}$ |
| Standard deviation of body diameters [m] | 6.35 × 10$^{-4}$ | 7.92 × 10$^{-5}$ |
| Ratio of body size standard deviation to the mean | 0.329 | 0.458 |
| Mean throat diameter [m] | 8.65 × 10$^{-4}$ | 7.89 × 10$^{-5}$ |
| Standard deviation of throat diameters [m] | 5.42 × 10$^{-4}$ | 4.52 × 10$^{-5}$ |
| Ratio of throat size standard deviation to the mean | 0.627 | 0.573 |
| Ratio of mean body size to mean throat size | 2.23 | 2.19 |
| Average coordination number | 6.75 | 6.94 |
| Average coordination number (excluding boundaries) | 6.37 | 6.51 |

cannot be accurately calculated from direct volume-averaging of the local viscosity values over the whole pore space, given the existence of interconnected preferential flow paths with varying cross-sections and the different viscosity values exhibited by the non-Newtonian fluid within the cross-section of a single pore. The approach followed in the current study consisted in reducing the whole range of local viscosities exhibited by the fluid within a single flow conduit to a unique efficient viscosity value. This was made possible by taking advantage of the regular geometries displayed by the extracted pore network, for which analytical solutions exist allowing for the modelling of the flow rate vs. pressure gradient relationships.

In the present pore network modelling approach, the porous matrix is considered as being a network of conduits [39,40]. Then, 1D analytical solutions of the relevant transport equations are solved inside the network by using finite difference schemes [41]. As reviewed by Blunt et al. [42], despite this simplification, many aspects of single and multiphase transport can be accurately predicted by using pore network modelling simulations. In order to perform the flow simulations, the files containing the geometrical information of the pore networks were first imported using OpenPNM [41].

If the simple case of the creeping flow of an incompressible fluid flowing through a cylindrical duct of cross-sectional area $A_i$ and length $L_i$ is considered, the hydraulic conductance $g_i$ can be expressed using Hagen-Poiseuille law:

$$g_i = \frac{1}{8}\left(\frac{A_i^2}{\pi L_i}\right) \tag{7}$$

In the currently considered networks, each conduit is composed of a series combination of 1/2 body - full throat – 1/2 body. The ratio between the pressure difference ($p_i - p_j$) and the flow rate $q_{ij}$ through a conduit connecting the pores i and j will be named $G_{ij}$, and can be calculated as:

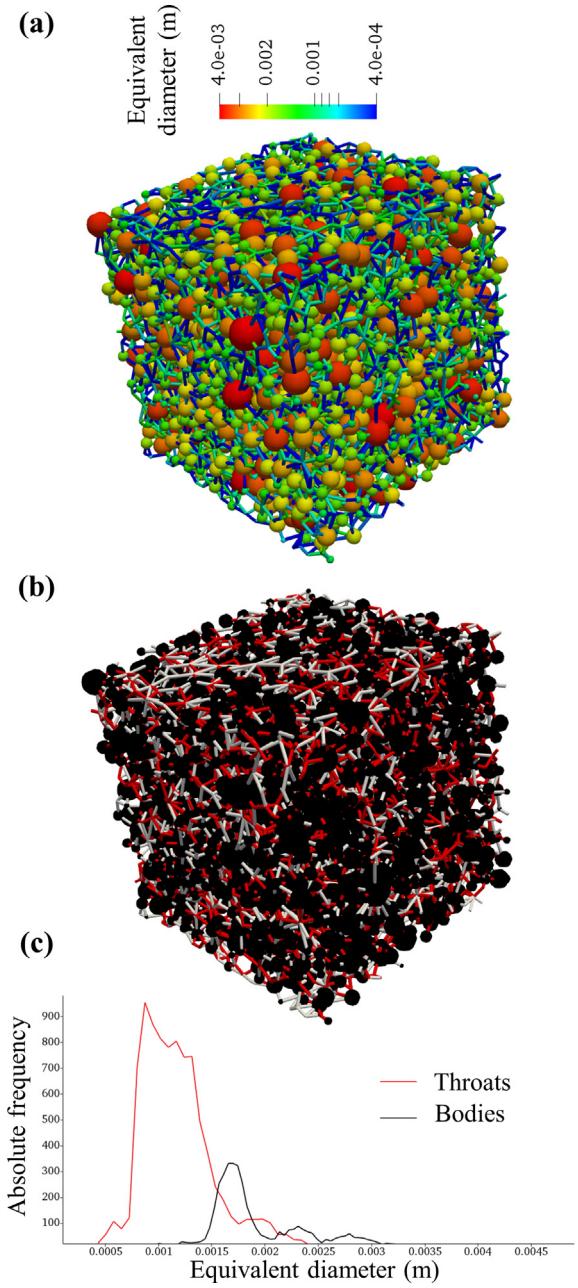


**Fig. 2.** Pore network model of the investigated pack of spherical beads with $d_s$ = 4-mm. (a) Image of the network as extracted from the 3D digital image. Warmer colors correspond to greater equivalent diameters of the pore bodies and pore throats. (b) Image representing the conducting and stagnant throats for the 700-ppm xanthan gum solution flowing at u = 3.67 × 10$^{-2}$ m/s. Black color represents pore bodies, red color represents conducting throats and white color represents stagnant throats. (c) Body size distribution and throat size distribution of the conducting throats. (For interpretation of the references to color in this figure legend, the reader is referred to the web version of this article.)

$$G_{ij} = \left( \frac{\mu_{eff,i}}{g_i \varepsilon_i} + \frac{\mu_{eff,ij}}{g_{ij} \varepsilon_{ij}} + \frac{\mu_{eff,j}}{g_j \varepsilon_j} \right)^{-1} \quad (8)$$

with $g_i$, $g_j$, $g_{ij}$ being the hydraulic conductances of the upstream half pore body, the downstream half pore body, and the pore throat, respectively. Analogously, $\mu_{eff,i}$, $\mu_{eff,j}$ and $\mu_{eff,ij}$ are the effective shear viscosities of the fluid in the upstream half pore body, the downstream half pore body, and the pore throat, respectively, and $\varepsilon_i$, $\varepsilon_j$. and $\varepsilon_{ij}$ are the corresponding shape factors. The following expression, based on Eq. (5), is used to calculate the values of $\mu_{eff,i}$, $\mu_{eff,j}$ and $\mu_{eff,ij}$.

$$\mu_{eff,k} = \text{Min}\left[ \mu_0, \mu_\infty + c\left(\frac{3n+1}{4n}\right)\left( \frac{\sqrt{\frac{A_k}{\pi}}\Delta P_k}{2cL_k} \right)^{\frac{n-1}{n}} \right] \text{ with } k = i, j, ij \quad (9)$$

In equations 9, $\Delta P_i$ represents the pressure drop between the center of the pore body i and the inlet of the throat ij, $\Delta P_j$ represents the pressure drop between the outlet of the throat ij and the center of the pore body j, and $\Delta P_{ij}$ is the pressure drop through the pore throat.

For the calculation of $g_i$, $g_j$ and $g_{ij}$, and subsequently $\mu_{eff,i}$, $\mu_{eff,j}$ and $\mu_{eff,ij}$ (equations (7) to (9)), the cross-sections of the conduits were considered to be circular, with varying diameter. The value of the cross-sectional area throughout each 1/2 body was calculated using the inscribed diameter of the pore body, and the cross-sectional area throughout each throat was equal to the boundary area between the connected pores, as provided by PoreSpy [38]. This boundary area corresponds to the surface of the intersection between the dilated volumes of two neighbor pores as provided by the SNOW algorithm [37]. The throat length $L_{ij}$ was equal to the center-to-center distance between pores less the inscribed radius of each neighboring pore body, and the body lengths $L_i$ and $L_j$ were equal to the inscribed radius of the connected pore bodies. The shape factors were introduced in Eq. (8) to take into account the non-circularity of the pore conduits, and are calculated in OpenPNM [41] by following the procedure described in the work of Akbari et al. [43]. In equations (9) to (11), the pressures at the inlet and the outlet of the throat obtained through interpolation of the pore pressures were used.

The flow rate through a given conduit $q_{ij}$ can be computed by using the following expression:

$$q_{ij} = G_{ij}(p_i - p_j) \quad (10)$$

with $p_i$ and $p_j$ being the pressure in the pore bodies i and j located at the inlet and the outlet of the throat, respectively. Therefore, the mass conservation equation over each pore i of the pore network is expressed as:

$$\sum_{j=1}^{Z} G_{ij}(p_i - p_j) = 0 \quad (11)$$

where Z is the number of pores and $G_{ij}$ is equal to zero when the pores i and j are not directly connected. The pressure field across the whole network can be calculated through application of the mass conservation equation to all pores with appropriate inlet and outlet boundary conditions. The system of equations was solved using the sparse solver included in the open-source software for mathematics, science, and engineering SciPy [44]. When applying the solver algorithm, the results obtained from a preliminary simulation with a Newtonian fluid were used as initial guess in each case for the computation of local viscosities. In the present simulations, two external faces of the investigated cubic volumes represented in Fig. 1(b) and 2(a) having their normal vector oriented in the same direction were chosen as the inlet and the outlet of the flow. Also, the value of the pressure of the pores located at the inlet face of the network was imposed as controlled boundary condition, while the pressure of the pores at the outlet face was kept constant. On this topic, Balhoff et al. [45] compared different numerical methods in terms of their stability, convergence and computation times when applied to simulate the flow of shear-thinning fluids in pore networks extracted from digital images of sandstones and packs of spheres.

### 3.4. Calculation of the average hydraulic tortuosity

The results of the flow simulations performed using the extracted pore networks were also used to quantify the hydraulic tortuosity of the flow paths, named T, observed during the flow of Newtonian and shear-thinning fluids through the pack of 4 mm beads and the sand pack. T is commonly defined as the ratio between the average length of the actual fluid flow path through the porous matrix, $L_e$, and the apparent length of the porous medium, L. In the absence of recirculation zones during the flow of an incompressible fluid, the surface average of $L_e/L$ weighted by the local flux over a reference surface perpendicular to the main flow direction is equivalent to the ratio between the surface average of the velocity magnitude field $|\bar{\mathbf{u}}|$ and the surface average of the component of velocity in the main flow direction $\bar{u}_x$ [46]. By taking the previous observation into account, T was calculated from the velocity maps obtained in the current simulations by using the following expression [14,46,47,48]:

$$T = \frac{|\bar{\mathbf{u}}|}{\bar{u}_x} \quad (12)$$

It should be mentioned that, if recirculation zones exist, T given by Eq. (12) corresponds to the upper limit of the surface average of $L_e/L$ weighted by the local flux.

## 4. Results and analysis

### 4.1. Percentage of conducting throats

The distribution of pore pressures was calculated by following the procedure described in subsection 3.3. From the pore pressure map, the effective throat viscosities $\mu_{eff,th}$ were computed by using Eq. (9). The individual flow rates through each throat were subsequently calculated with Eq. (10). It was observed that the value of the flow rate was very low in an important number of throats. The group of "stagnant" throats were formed to a great extent by the throats with the smallest equivalent diameters. Also, the throats being oriented nearly perpendicularly to the main flow direction presented very small pressure gradients, and therefore very high values of $\mu_{eff,th}$ resulting in negligible flow rates. In the further analysis, the throats in which the flow rate was lower than 10% of the average flow rate (arbitrary value) will be referred to as "stagnant throats", and the rest of the throats will be named "conducting throats". An example of the stagnant and conducting throats in the pack of 4 mm spheres is represented in Fig. 2(b).

The amount and percentage of conducting throats under different u values were calculated and listed for the flow of the three investigated fluids through the pack of 4 mm spheres, and the results are listed in Table 3. It can be observed that the percentage of conducting throats it almost constant (59 ± 2%) for the considered range of u and $C_p$. The slightly lower percentage of conducting throats reported for the higher values of $C_p$ resulted from a more pronounced shear-thinning behaviour (lower values of n), which favors more strongly the flow in the main flow direction as reported by Fadili et al. [49]. The percentage of conducting throats was also computed for the flow of the 500 ppm polymer solution through the sand pack, as listed in Table 4, and the obtained values

**Table 3**
Amount and percentage of conducting throats for different values of u and $C_p$ during the flow of the shear-thinning fluids through the pack of 4 mm spheres. The deviations from the listed average values of u are due to slight differences between the considered u values for each $C_p$.

| Porous medium | $C_p$ (ppm) | Total number of throats | Number of conducting throats u = 3.30 × $10^{-3}$ ± 6 × $10^{-4}$ m/s | Number of conducting throats u = 1.70 × $10^{-2}$ ± 1 × $10^{-3}$ m/s | Number of conducting throats u = 3.30 × $10^{-2}$ ± 4 × $10^{-3}$ m/s |
|---|---|---|---|---|---|
| Pack of spheres 4 mm | 200 | 15,417 | 9337 (60.56%) | 9411(61.04%) | 9431 (61.17%) |
| | 500 | | 8987 (58.29%) | 9109 (59.08%) | 9160 (59.41%) |
| | 700 | | 8807 (57.13%) | 8973 (58.20%) | 9034 (58.60%) |

were very close to those reported for the pack of spheres (~55%). No significant increase in the number of conducting throats was associated to an increase in u. Given the weak effects of u and $C_p$, it can be expected that the amount of conducting throats mainly depends on the distribution of equivalent throat diameters and the coordination number of the pore bodies.

For the sake of comparison with the characteristics of the whole pore networks, some important microstructural features of the conducting network (excluding the stagnant pores) are listed in Table 5. The case of the 500-ppm solution flowing through the pack of 4 mm spheres and the sand pack was used for the calculation of the conducting network features. Through comparison of tables 2 and 5, it is noticed that the mean throat and body sizes of the conducting pores are greater than the mean sizes of all pores. This difference is more marked in the case of the throat size, which seems reasonable given that it is the size of pore constrictions which limits to a greater extent the equivalent conductance of pores. Also, the throat and bodies sizes are more narrowly distributed when only the conducting pores are considered, given the exclusion of the smallest sizes. A remarkable feature of this comparison is that the average coordination number of the conducting network is significantly lower than the one of the whole network.

**Table 5**
Essential microstructural features of the conducting pores. The listed values were obtained for the flow of the 500-ppm solution under injection velocities of 3.04 × $10^{-2}$ m/s for the pack of 4 mm spheres and 1.97 × $10^{-3}$ m/s for the sand pack.

| Sample | Pack of spheres (4 mm) | Sand pack |
|---|---|---|
| Mean body diameter of conducting pores [m] | 1.99 × $10^{-3}$ | 1.90 × $10^{-4}$ |
| Standard deviation of body diameters of conducting pores [m] | 5.98 × $10^{-4}$ (30.05% of the mean) | 7.45 × $10^{-5}$ (39.21% of the mean) |
| Ratio of body size standard deviation to the mean of conducting pores | 0.301 | 0.392 |
| Mean throat diameter of conducting pores [m] | 1.19 × $10^{-3}$ | 1.03 × $10^{-4}$ |
| Standard deviation of throat diameter of conducting pores [μm] | 3.69 × $10^{-4}$ (31.01% of the mean) | 3.96 × $10^{-5}$ (38.44% of the mean) |
| Ratio of throat size standard deviation to the mean of conducting pores | 0.310 | 0.384 |
| Ratio of mean body size to mean throat size of conducting pores | 1.67 | 1.84 |
| Average coordination number of conducting pores | 4.27 | 4.48 |
| Average coordination number of conducting pores (excluding boundaries) | 4.20 | 4.70 |

### 4.2. Upscaling shear viscosity: From local viscosities to Darcy viscosity

The $\mu_{eff,th}$ distributions corresponding to the injection of the three investigated fluids through the pack of 4 mm spheres under different values of u were computed and are represented in Fig. 3. In the same manner, the $\mu_{eff,th}$ distributions for the injection of the 500-ppm polymer solution through the sand pack are represented in Fig. 4. Only the conducting throats were considered in these figures. This is consistent with the previous results of López [3], who reported that the pores in which the fluid exhibits very high viscosity values, have little impact on the macroscopic viscosity. The values of $\mu_D$ were also displayed in Figs. 3 and 4 for comparison.

The peaks displayed in Fig. 3 and Fig. 4 represent the most frequent values of efficient viscosity $\mu_{eff,th}$ in the throats of the pore conduits for different combinations of polymer concentration and Darcy velocity. Fig. 3 shows that the peak of the $\mu_{eff,th}$ is practically identical to $\mu_D$ in all cases for the pack of spheres. This means that the macroscopic $\mu_D$ value corresponds to the most frequent local $\mu_{eff,th}$ value in the conducting throats. Apart from this, the distributions of $\mu_{eff,th}$ are shifted towards the smaller values, similarly to the throat size distributions displayed in Fig. 2(c). Another significant feature is that the range of viscosities exhibited by the fluid was wider at the lowest injection velocities and for the most concentrated polymer solutions (lower n).

By observing Fig. 4, which corresponds to the sand pack, it can be noticed that the value of $\mu_D$ is slightly lower than the most frequent local $\mu_{eff,th}$. This may be stem from the wider dispersion of the body and throats sizes distributions as compared to the pack of spheres (as shown in Table 5). Indeed, the body and throat size distributions overlap to a larger extent in the case of the sand pack, as displayed in Fig. 1(c). Consequently, the value of $\mu_D$ is expected to be more sensitive to the values of local viscosities in the pore bodies (lower than in the throats) than in the case of the pack of spheres, which results in a shift to the left of $\mu_D$ with respect to the $\mu_{eff,th}$ maximum in Fig. 4. To illustrate this point, the distribution of local viscosities in the throats and in the upstream and downstream bodies are represented in Fig. 5 for the flow of the 500-ppm solution through both porous media. It can be deduced from this figure that the body viscosities are closer to the throat viscosity in the case of the pack of spheres, which is consistent with the previous observations.

From the previous observations, it can be concluded that the value of $\mu_D$ is intimately related to the viscosity exhibited by the fluid in the conducting conduits. It should be noted that, for a simple bundle of capillaries, Darcy viscosity can be computed from the flow-rate weighted average of the local viscosity values. Therefore, with the objective to propose an analytical expression allowing for the calculation of $\mu_D$ from the local viscosities in the conduits, it seems reasonable to consider a flow-rate weighted average of the local viscosities. Also, the viscosity in the pore bodies of each

**Table 4**
Amount of percentage of conducting throats for different values of u during the flow of the shear-thinning fluids through the sand pack.

| Porous medium | $C_p$ (ppm) | Total number of throats | Number of conducting throats u = 1.00 × $10^{-9}$ m/s | Number of conducting throats u = 2.81 × $10^{-6}$ m/s | Number of conducting throats u = 1.97 × $10^{-3}$ m/s |
|---|---|---|---|---|---|
| Sand pack | 500 | 28,713 | 15,789 (54.98%) | 15,791 (55.00%) | 16,240 (56.56%) |

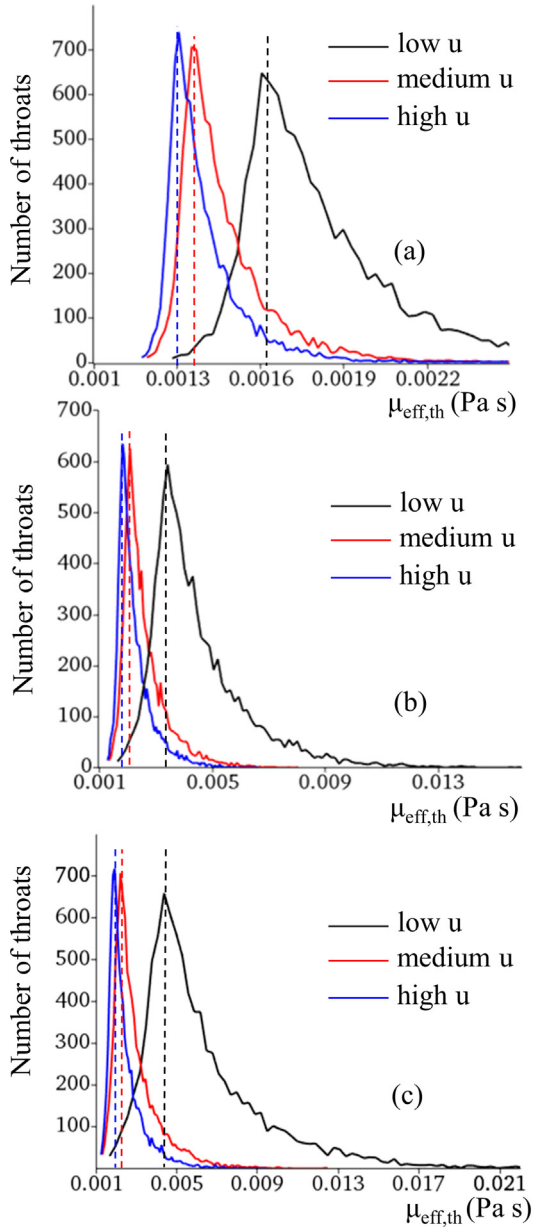


**Fig. 3.** Distribution of $\mu_{eff,th}$ values throughout the pack of 4 mm spheres under different values of u and $C_p$. Low, medium and high u correspond to u = 3.30 × $10^{-3}$ ± 6 × $10^{-4}$ m/s, u = 1.80 × $10^{-2}$ ± 1 × $10^{-3}$ m/s and u = 3.09 × $10^{-2}$ ± 5 × $10^{-4}$ m/s, respectively (deviations from the average value are due to slight differences between the considered u values for each $C_p$). Black, red, and blue vertical dashed lines correspond to the values of Darcy viscosity for the low, medium and high values of u, respectively. (a) $C_p$ = 200 ppm. (b) $C_p$ = 500 ppm. (c) $C_p$ = 700 ppm. (For interpretation of the references to color in this figure legend, the reader is referred to the web version of this article.)

conduit proved to be significant, especially in the cases in which the body and throat size distributions overlap. Consequently, the representative viscosity of each conduit should take into account the viscosities in both pore bodies connected by the considered throat as well as the viscosity in the throat itself. For these reasons, the flow-rate averaged viscosity $\bar{\mu}_q$ was calculated in the present experiments under different boundary conditions using the following expression:

$$\bar{\mu}_q = \frac{\sum_{y=1}^{N_t} q_y \mu_{eff,conduit_y}}{\sum_{y=1}^{N_t} q_y} \quad (13)$$

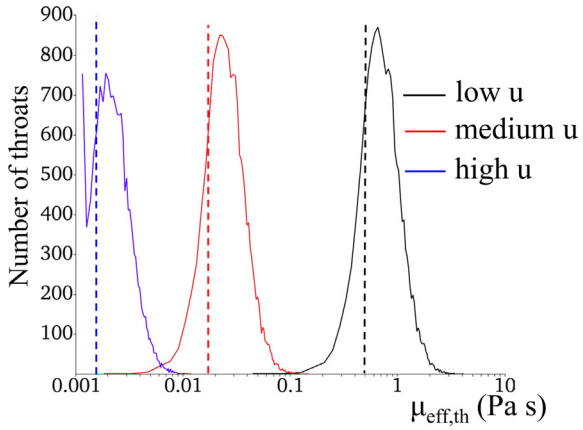


**Fig. 4.** Distribution of $\mu_{eff,th}$ values for the flow of the 500 ppm polymer solution through the sand pack under different values of u. Low, medium and high u correspond to u = 1.00 × $10^{-9}$, u = 2.81 × $10^{-6}$ m/s and u = 9.42 × $10^{-4}$ m/s, respectively. Black, red, and blue vertical dashed lines correspond to the values of Darcy viscosity for the low, medium and high values of u, respectively. (For interpretation of the references to color in this figure legend, the reader is referred to the web version of this article.)

with $q_y$ being the flow rate through the body-throat-body conduit y and $N_t$ being the total number of conduits in the network. $\mu_{eff,conduit_y}$ was calculated as the arithmetic mean of the viscosity values obtained in the different stretches of the conduit y, i.e., the mean of the viscosities in the upstream body, the throat, and the downstream body.

Several pore network flow simulations were conducted in which the values of $\bar{\mu}_q$ (from Eq. (13)) and $\mu_D$ (from Eq. (6)) were computed and compared. A first set of simulations considered the injection of the same 500-ppm solution through the pack of 4 mm spheres and through the sand pack. Table A1, presented in the Appendix, shows that the obtained values of $\bar{\mu}_q$ are extremely close to the values $\mu_D$ in all cases, with differences lower than 3.3%. This means that $\mu_D$ can be successfully predicted from the local scale viscosities by using the analytical expression given by Eq. (13), i.e., .$\bar{\mu}_q$ $\mu_D$ for the considered media.

In order to confirm the validity of Eq. (13) to predict $\mu_D$, a second set of simulations assessed the accuracy of the predictions for the flow of the 500 ppm solutions through 4 packs of equal spheres of 1 mm, 2 mm, 3 mm and 4 mm diameter, respectively. The results reported in Table A2 of the Appendix show that the use of Eq. (13) to predict $\mu_D$ is appropriate independently of the size of the spheres, and therefore of the permeability of the pack of beads. Furthermore, a third set of simulations were devoted to the comparison of $\bar{\mu}_q$ and $\mu_D$ for the injection of the three polymer solutions through the same pack of 4 mm spherical beads (these results are not shown in the manuscript). The observed differences between $\bar{\mu}_q$ and $\mu_D$ were always lower than 2.5%, so the approach is valid for the three shear-thinning fluids.

### 4.3. Average shear viscosity for each throat size

The dependency of the local throat viscosities on the value of the equivalent throat diameter $d_{th}$ could also be quantified from the results of the flow simulations. To do so, the average value of $\mu_{eff,th}$ in the throats of a given size class, named $\bar{\mu}_{eff,th}$, was calculated for the flow through the pack of 4 mm spheres and the results were plotted in Fig. 6. The $\bar{\mu}_{eff,th}$ vs. $d_{th}$ datasets were fitted by a linear function, which displayed in the same figure together with the

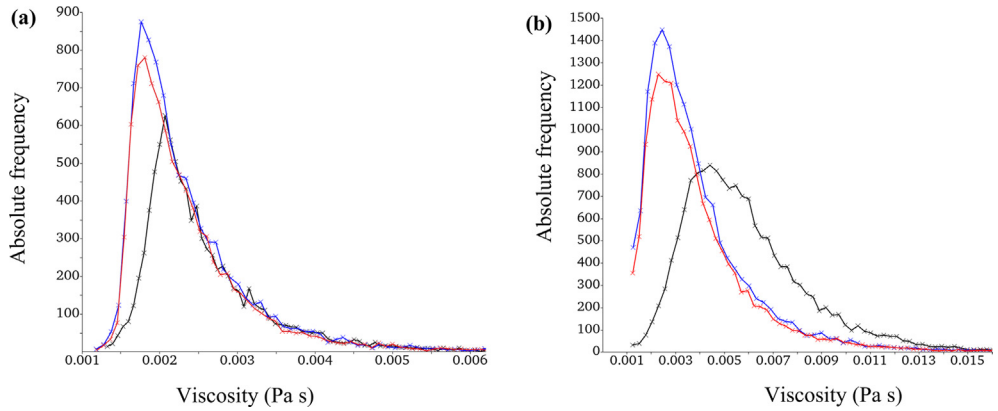


**Fig. 5.** Distribution of local viscosities in the throats (dark colors) and in the upstream and downstream bodies of the body-throat-body conduits (blue and red colors) for the 500-ppm polymer solution. (a) Pack of 4 mm spheres. (b) Sand pack. (For interpretation of the references to color in this figure legend, the reader is referred to the web version of this article.)

obtained average errors E between the fitting function and the data. The reported values of E were lower than 2.5% in all cases. It can be noticed that, independently of the considered value of $C_p$ and u, $\bar{\mu}_{eff,th}$ tends to decrease as $d_{th}$ increases. This means that, in general, shear-thinning fluids display higher viscosities in the small pores, which is predicted by Eq. (5). The slope of the fitted linear functions is higher at the lowest injection velocities, reflecting a pronounced shear-thinning behavior. In contrast, lower slopes are reported for the higher flow velocities, which is explained by the attenuation of shear-thinning effects once the values of local viscosities approach the Newtonian viscosity plateau at high shear rates. These observations are confirmed for the investigated three fluids, with the only significant difference being the range of $\bar{\mu}_{eff,th}$ covered depending on the $C_p$ of the polymer solution.

### 4.4. Tortuosity during the flow of shear-thinning fluids

The average hydraulic tortuosity T was calculated for a set of numerical simulations by following the procedure presented in subsection 3.4. First, the flows of the considered shear-thinning fluids and water through the pack of 4 mm spheres were simulated. The same range of u used in the experimental works of Rodríguez de Castro and Radilla [33] was used. Then, the flows of the 500-ppm solution and water through the sand pack were simulated by considering a wider range of u covering more than 4 orders of magnitude. The T vs. u relationships obtained from these numerical simulations are displayed in Fig. 7.

Fig. 7(a) shows that, contrarily to the case of the Newtonian fluid (water), T depends on u for the flow of shear-thinning fluids. This dependency is stronger as the shear-thinning behaviour becomes more pronounced (higher values of $C_p$). These results are in good agreement with the previous numerical results dealing with the flow of yield stress fluids through 2D porous media [14]. The tortuosity of the streamlines is always lower in the case of the shear-thinning fluid as compared to the Newtonian fluid, which is due to the directional nature of shear-thinning behavior. In other words, the flow of a shear-thinning fluid is extremely penalized in the directions of low-pressure gradient (e.g., when the axial direction of a conduit is perpendicular to the main flow direction), as can be deduced from Eq. (5), which results in increased straightness of the flow paths. Such a reduction of T becomes less significant as u is increased, because of the increasing number of pores in which the fluid exhibits the Newtonian plateau viscosity value $\mu_\infty$.

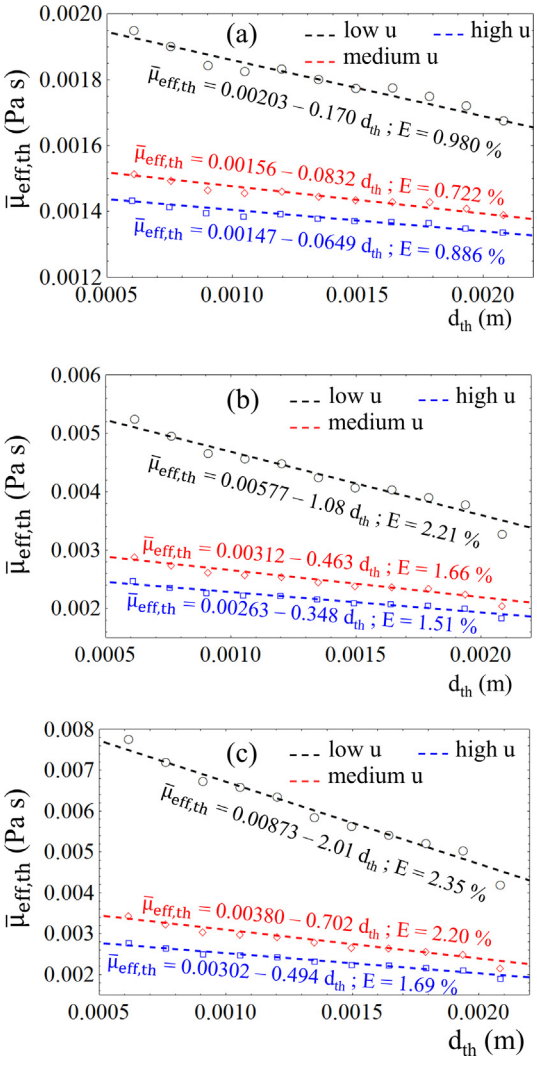


**Fig. 6.** Average effective throat viscosity $\bar{\mu}_{eff,th}$ for each pore throat size during the flow of the three investigated fluids through the pack of 4 mm spheres under different values of u. (a) 200 ppm solution.(b) 500 ppm solution. (c) 700 ppm solution. Low, medium and high u correspond to u = $3.30 \times 10^{-3} \pm 6 \times 10^{-4}$ m/s, u = $1.80 \times 10^{-2} \pm 1 \times 10^{-3}$ m/s and u = $3.09 \times 10^{-2} \pm 5 \times 10^{-4}$ m/s, respectively (deviations from the average value are due to slight differences between the considered u values for each $C_p$). All data sets were fitted by a linear function, which is displayed in the figure (dashed lines) together with the average error of the fit E.

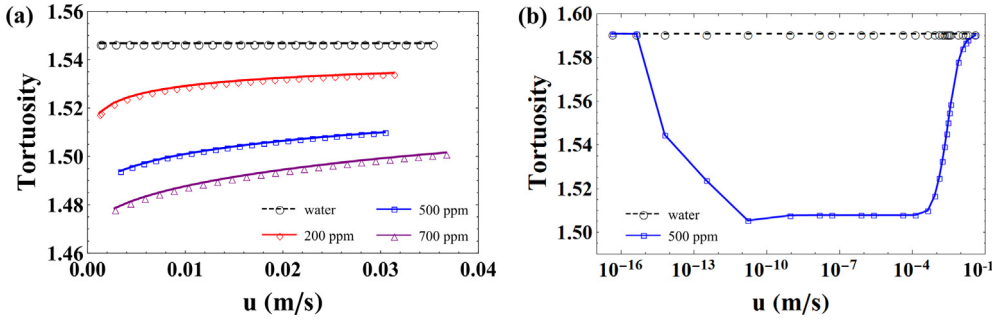


**Fig. 7.** Average hydraulic tortuosity of the streamlines as a function of Darcy velocity u. (a) Flow through the pack of 4 mm spheres. (b) Flow through the sand pack.

A thorough assessment of the dependency of T on u, covering a wide range of u, can be undertaken from the results reported in Fig. 7(b) for the 3D sand pack. In the same manner as for the pack of spheres, T decreased when increasing u, and some supplementary conclusions can be drawn. First, the value of T for the shear-thinning fluid attains the Newtonian hydraulic tortuosity value when the injection velocity is extremely high. The analysis of the viscosity distribution in the pores at the highest values of u (not shown in the manuscript) revealed that the fluid exhibited the high-shear-rates Newtonian plateau viscosity value $\mu_\infty$ in almost all pores, which is consistent with the previous observation. Second, the value of T at the lowest injection velocities is also equal to the Newtonian tortuosity value, which resulted from the fluid exhibiting a viscosity equal to the low-shear-rates Newtonian plateau viscosity value $\mu_0$ in almost all pores. Third, a plateau of low tortuosity was reported as the injection velocity was varied between $10^{-3}$ m/s and $10^{-11}$ m/s. In this case, the whole distribution of viscosities fell between the plateau values $\mu_\infty$ and $\mu_0$.

It can be concluded that the dependency of T on u exists only within the range of u in which the shear-thinning fluid exhibits a Newtonian plateau viscosity in certain pores, but not in all pores. These results are consistent with the results of the numerical simulations performed by Bao et al. [13] for the flow of truncated power-law fluids in rough-walled fractures. Another significant observation is that similar T vs. u curves were obtained for the pack of spheres and the sand pack when plotted on the same scale, as shown in the Figure S1 of the supplementary material.

An additional set of numerical experiments was conducted in order to assess the effect of the value of $\mu_0$ on the number of conducting throats and the T vs. u relationship. To do so, the injection of the three polymer solutions through the pack of 4 mm beads was simulated by using $\mu_0$ = 0.002 Pa s for 200 ppm, $\mu_0$ = 0.007 P a s for 500 ppm and $\mu_0$ = 0.014 Pa s for 700 ppm [3] while keeping the original values of c, n and $\mu_\infty$ listed in Table 1. It was observed that the percentage of conducting throats at the lowest values of u was very close to those listed in Table 3. However, the decrease in the value of $\mu_0$ produced an increase in T at the lowest injection velocities (as in the case of the sand pack), which is not observed in Fig. 7a. The T vs. u relationship provided by this second set of experiments was compared to the original one in Figure S2 of the supplementary material.

## 5. Conclusions

Representative pore networks were extracted from 3D digital images of a pack of spheres [31] and a sand pack [32]. Then, the flow of different shear-thinning fluids was simulated through these pore networks allowing for the computation of local viscosity and flow rate maps. The analysis of the distribution of viscosities within the active channels led to the following conclusions:

- For packs of equal spheres, the value of macroscopic Darcy viscosity matches the most frequent local viscosity value in the conducting pore throats. This is in contrast with previous research in which the non-conducting throats were not excluded from the distribution of local viscosities [3]. Moreover, a linear decrease in the average local viscosity exhibited by the fluid in the pore throats of a given size class is observed as the considered throat size is increased.
- Darcy viscosity is sensitive to the values of local viscosities in the pore bodies for the sand pack, due to overlap between the pore body and pore throat size distributions.

Furthermore, an expression to calculate Darcy viscosity from the local viscosity distribution was proposed and validated in both unconsolidated media (Eq. (13)), filling a gap in the literature [9,12,17–23]. By using this expression, Darcy viscosity was accurately calculated independently of the permeability of the pack of spheres and the Carreau model parameters.

Additional results showed that the average hydraulic tortuosity depends on u for the flow of shear-thinning fluids through 3D porous media. Such dependence exists only within the range of injection velocities in which the shear-thinning fluid exhibits a Newtonian plateau viscosity in certain pores, but not in all pores. Moreover, the directional nature of shear-thinning behavior resulted in decreased tortuosity values as compared to the flow of Newtonian fluids, in agreement with previous results in 2D media [14] and rough-walled fractures [13].

The current study provided valuable insight into the interplay between microstructural characteristics, local shear rheology and macroscopic quantities. The gained knowledge of pore-scale mechanisms is expected to improve the decision algorithms used to optimize the process conditions in many industrial situations in which non-Newtonian fluids are involved, including biomedical [6,7,50] and environmental applications [5]. However, taking into account the evolving microstructure exhibited by the living tissues involved in biomedical research remains a challenge. On this subject, Ezeuko et al. [51] developed a pore network simulator for modeling biofilm evolution in porous media. The model used by the preceding authors implemented a modified form of the classical Poiseuille equation in the pore network simulations to account for the presence of porous biofilms within the flow channels [52]. Moreover, future works are required to extend the present results to consolidated porous media and fluids with different constitutive equations, such as Meter and Ellis models.

The effects of viscoelasticity and yield stress should be specifically evaluated, as they are not negligible for many shear-thinning fluids [53]. In particular, polymer coils often stretch under high flow rates during extensional flow of viscoelastic polymer solutions. Such stretching makes the flow unstable and causes irregular secondary flow resulting in elastic turbulence [54]. By means of particle image velocimetry experiments performed in a

microfluidic device, Ekanem et al. [55] showed that the elastic turbulence effect occurs within a single pore throat with no flow history. Also, Browne et al. [56] proved that unstable eddies form upstream of pore constrictions when the pore spacing is large, while switching between two distinct unstable flow states occur when pore spacing is sufficiently small. Future works should investigate how to take into account viscoelastic effects and the effective behavior of elastic turbulence in the pore network simulations. Furthermore, it should be noted that pure shear has been assumed in the present flow model. Nevertheless, flows present both a shear and an extensional component in many real applications. Zamani et al. [57] numerically showed that aspect ratio plays an important role on the local rheology exhibited by non-Newtonian fluids, and the work of van den Ende [58] provided some expressions allowing for the computation of the total pressure drops through a sinusoidal tube from the sum of the shear and elongational contributions to pressure drop. It is worth considering the use of these expressions to extend the current viscosity upscaling approach to situations in which pure shear flow does not apply.

Several high-molecular-weight bio polymers are not only shear-thinning, but also show shear-thickening effects related to elastic turbulence [59]. In this regard, Shende et al. [60] recently proposed an empirical equation to express the viscosity of typical shear-thickening fluids as a function of shear stress over a wide range of shear stresses, covering the viscosity plateau, the shear-thinning, and the shear-thickening regions. Future research efforts may be devoted to the implementation of this empirical equation in the pore network simulations presented in this work.

## CRediT authorship contribution statement

**Antonio Rodríguez Castro:** Conceptualization, Methodology, Formal analysis, Investigation, Writing - original draft, Visualization. **Benoit Goyeau:** Formal analysis, Writing - review & editing.

## Declaration of Competing Interest

The authors declare that they have no known competing financial interests or personal relationships that could have appeared to influence the work reported in this paper.

## Appendix A. Supplementary data

Supplementary data to this article can be found online at https://doi.org/10.1016/j.jcis.2021.01.081.

## References


[1] R.P. Chhabra, J.F. Richardson, Non-Newtonian Flow and Applied Rheology: Engineering Applications (Butterworth-Heinemann/IChemE), 2nd Edition., 2008.
[2] Ch. Airiau, A. Bottaro, Flow of shear-thinning fluids through porous media, Adv. Water Resour. 143 (2020) 103658.
[3] X. López, Pore-scale modelling of non-Newtonian flow, PhD thesis, Dep. of Earth Sci, Group, Imperial College, London, 2004.
[4] S. Berg, J. van Wunnik, Shear Rate Determination from Pore-Scale Flow Fields, Transp. Porous Media 117 (2) (2017) 229–246.
[5] S.C. Hauswirth, C.A. Bowers, C.P. Fowler, P.B. Schultz, A.D. Hauswirth, T. Weigand, C.T. Miller, Modeling cross model non-Newtonian fluid flow in porous media, J. Contam. Hydrol. 235 (2020) 103708.
[6] S.C. Cowin, L. Cardoso, Blood and interstitial flow in the hierarchical pore space architecture of bone tissue, J. Biomech. 48 (5) (2015) 842–854.
[7] K. Chandran, I.S. Dalal, K. Tatsumi, K. Muralidhar, Numerical simulation of blood flow modeled as a fluid- particulate mixture, J. Nonnewton. Fluid Mech. 285 (2020) 104383.
[8] G. Chauveteau, Rodlike polymer solution flow through fine pores: Influence of pore size on rheological behavior, J. Rheol. 26 (1982) 111.
[9] X. López, P.H. Valvatne, M.J. Blunt, Predictive network modeling of single-phase non-Newtonian flow in porous media, J. Colloid Interface Sci. 264 (1) (2003) 256–265.
[10] A. Rodríguez de Castro, M. Agnaou, Numerical Investigation of the Apparent Viscosity Dependence on Darcy Velocity During the Flow of Shear-Thinning Fluids in Porous Media, Transp. Porous Media 129 (2019) 93–120.
[11] U. Eberhard, H.J. Seybold, M. Floriancic, P. Bertsch, J. Jiménez-Martínez, J.S. Andrade, M. Holzner, Determination of the Effective Viscosity of Non-newtonian Fluids Flowing Through Porous Media, Front. Phys. 7 (2019) 71.
[12] A.F. Morais, H. Seybold, H.J. Herrmann, J.S. Andrade, Non-Newtonian Fluid Flow through Three-Dimensional Disordered Porous Media, Phys. Rev. Lett. 103 (19) (2009) 194502.
[13] K. Bao, A. Lavrov, H.M. Nilsen, Numerical modeling of non-Newtonian fluid flow in fractures and porous media, Comput. Geosci. 21 (5–6) (2017) 1313–1324.
[14] A. Rodríguez de Castro, M. Agnaou, A. Ahmadi-Sénichault, A. Omari, Numerical investigation of Herschel-Bulkley fluid flows in 2D porous media: yielding behaviour and tortuosity, Comput. Chem. Eng. 140 (2020) 106922.
[15] T. Sochi, Analytical solutions for the flow of Carreau and Cross fluids in circular pipes and thin slits, Rheologica Acta 54 (2015) 745–756.
[16] H. Dong, M.J. Blunt, Pore-network extraction from micro-computerized-tomography images, Phys. Rev. E 80 (3) (2009) 036307.
[17] T. Sochi, M.J. Blunt, Pore-scale network modeling of Ellis and Herschel-Bulkley fluids, J. Petrol. Sci. Eng. 60 (2) (2008) 105–124.
[18] T. Sochi, Flow of Non-Newtonian Fluids in Porous Media, J. Polym. Sci., Part B: Polym. Phys. 48 (2010) 2437–2767.
[19] M.T. Balhoff, K.E. Thompson, A macroscopic model for shear-thinning flow in packed beds based on network modeling, Chem. Eng. Sci. 61 (2006) 698–719.
[20] C.D. Tsakiroglou, A methodology for the derivation of non-Darcian models for the flow of generalized Newtonian fluids in porous media, J. Nonnewton. Fluid Mech. 105 (2002) 79–110.
[21] C.D. Tsakiroglou, Correlation of the two-phase flow coefficients of porous media with the rheology of shear-thinning fluids, J. Nonnewton. Fluid Mech. 117 (2004) 1–23.
[22] C.L. Perrin, P.M.J. Tardy, K.S. Sorbie, J.C. Crawshaw, Experimental and modeling study of Newtonian and non-Newtonian fluid flow in pore network micromodels, J. Colloid Interface Sci. 295 (2) (2006) 542–550.
[23] S. Aghabozorgi, B. Rostami, An Investigation of Polymer Adsorption in Porous Media Using Pore Network Modelling, Transp. Porous Media 115 (2016) 169–187.
[24] U. Eberhard, H.J. Seybold, E. Secchi, J. Jiménez-Martínez, P.A. Rühs, A. Ofner, M. Holzner, Mapping the local viscosity of non-Newtonian fluids flowing through disordered porous structures, Sci. Rep. 10 (1) (2020) 11733.
[25] P.J. Carreau, Rheological equations from molecular network theories, Transactions of the Society of Rheology 16 (1972) 99–127.
[26] A.S. Lodge, Constitutive equations from molecular network theories for polymer solutions, Rheologica Acta 7 (4) (1968) 379–392.
[27] S.K. Kim, Flow-rate based method for velocity of fully developed laminar flow in tubes, J. Rheol. 62 (6) (2018) 1397–1407.
[28] T. Shende, V.J. Niasar, M. Babaei, Effective viscosity and Reynolds number of non-Newtonian fluids using Meter model, Rheologica Acta (2020). In press.
[29] A. Rodríguez de Castro, G. Radilla, Non-Darcian flow experiments of shear-thinning fluids through rough-walled rock fractures, Water Resour. Res. 52 (2016) 9020–9035.
[30] J.L. Finney, Random Packings and the Structure of Simple Liquids. I. The Geometry of Random Close Packing, Proceedings of the Royal Society of London A 319 (1970) 479–493.
[31] J. Finney, "Finney Packing of Spheres." Digital Rocks Portal, Digital Rocks Portal, 15 April 2016, http://www.digitalrocksportal.org/projects/47 Accessed 5 Dec. 2020.
[32] A. Sheppard, M. Prodanovic, Network Generation Comparison Forum. Digital Rocks Portal, 2015. [Online]. Available: http://www.digitalrocksportal.org/projects/16 Accessed 5 Dec. 2020.
[33] A. Rodríguez de Castro, G. Radilla, Non-Darcian flow of shear-thinning fluids through packed beads: experiments and predictions using Forchheimer's law and Ergun's equation, Adv. Water Resour. 100 (2017) 35–47.
[34] K.A. Brookshier, J.M. Tarbell, Evaluation of a transparent blood analog fluid: aqueous xanthan gum/glycerin, Biorheology 30 (1993) 107–116.
[35] F.J.H. Gijsen, E. Allanic, F.N. van de Vosse, J.D. Janssen, The influence of the non-Newtonian properties of blood on the flow in large arteries: unsteady flow in a 90° curved tube, J. Biomech. 32 (7) (1999) 705–713.
[36] X. Yang, Y. Mehmani, W.A. Perkins, A. Pasquali, M. Schönherr, K. Kim, M. Perego, M.L. Parks, N. Trask, M.T. Balhoff, M.C. Richmond, Intercomparison of 3D pore-scale flow and solute transport simulation methods, Adv. Water Resour. 95 (2016) 176–189.
[37] J.T. Gostick, Versatile and efficient pore network extraction method using marker-based watershed segmentation, Phys. Rev. E 96 (2017) 023307.
[38] J.T. Gostick, Z.A. Khan, T.G. Tranter, M.D. Kok, M. Agnaou, M. Sadeghi, R. Jervis, PoreSpy: A Python Toolkit for Quantitative Analysis of Porous Media Images, Journal of Open Source Software 4 (2019) 1296.
[39] M.J. Blunt, Flow in Porous Media —Pore-Network Models and Multiphase Flow, Curr. Opin. Colloid Interface Sci. 6 (2001) 197–207.
[40] V. Joekar-Niasar, S.M. Hassanizadeh, Analysis of Fundamentals of Two-Phase Flow in Porous Media Using Dynamic Pore-Network Models: A Review, Critical Reviews in Environmental Science & Technology 42 (2012) 1895–1976.

[41] J. Gostick, M. Aghighi, J. Hinebaugh, T. Tranter, M.A. Hoeh, H. Day, B. Spellacy, M.H. Sharqawy, A. Bazylak, A. Burns, W. Lehnert, OpenPNM: a pore net- work modeling package, Comput. Sci. Eng. 18 (2016) 60–74.
[42] M.J. Blunt, B. Bijeljic, H. Dong, O. Gharbi, S. Iglauer, P. Mostaghimi, A. Paluszny, Ch. Pentland, Pore-scale imaging and modelling, Adv. Water Resour. 51 (2013) 197–216.
[43] M. Akbari, D. Sinton, M. Bahrami, Viscous flow in variable cross-section microchannels of arbitrary shapes, Int. J. Heat Mass Transf. 54 (2011) 3970–3978.
[44] E. Jones, T. Oliphant, P. Peterson, SciPy: Open source scientific tools for Python (2001); available at http://www.scipy.org/.
[45] M. Balhoff, D. Sanchez-Rivera, A. Kwok, Y. Mehmani, M. Prodanović, Numerical Algorithms for Network Modeling of Yield Stress and other Non-Newtonian Fluids in Porous Media, Transp. Porous Media 93 (2012) 363–379.
[46] A. Duda, Z. Koza, M. Matyka, Hydraulic tortuosity in arbitrary porous media flow, Phys. Rev. E 84 (3) (2011) 036–319.
[47] J. Zhao, Q. Kang, J. Yao, H. Viswanathan, R. Pawar, L. Zhang, H. Sun, The effect of wettability heterogeneity on relative permeability of two-phase flow in porous media: a lattice Boltzmann study, Water Resour. Res. 54 (2) (2018) 1295–1311.
[48] M. Zhang, M. Prodanovic, M. Mirabolghasemi, J. Zhao, 3D Microscale Flow Simulation of Shear-Thinning Fluids in a Rough Fracture, Transp. Porous Media 128 (2019) 243–269.
[49] A. Fadili, P. M. J. Tardy, J. R. Anthony Pearson, A 3D filtration law for power-law fluids in heterogeneous porous media, Journal of Non-Newtonian Fluid Mechanics 106(2-3) (2002) 121–146.
[50] C. Beauchesne, M. Chabanon, B. Smaniotto, B. Ladoux, B. Goyeau, B. David, Channeling Effect and Tissue Morphology in a Perfusion Bioreactor Imaged by X-Ray Microtomography, Tissue Engineering and Regenerative Medicine 17 (2020) 301–311.
[51] C.C. Euzeko, A. Sen, A. Grigoryan, I.D. Gates, Pore-Network Modeling of Biofilm Evolution in Porous Media, Biotechnol. Bioeng. 108 (10) (2011) 2413–2423.
[52] M. Thullner, J. Zeyer, K. Wolfgang, Influence of microbial growth on hydraulic properties of pore networks, Transp. Porous Media 49 (2002) 99–122.
[53] S. De, P. Krishnan, J. van der Schaaf, J.A.M. Kuipers, E.A.J.F. Peters, J.T. Padding, Viscoelastic effects on residual oil distribution in flows through pillared microchannels, J. Colloid Interface Sci. 510 (2018) 262–271.
[54] A. Groisman, V. Steinberg, Elastic turbulence in a polymer solution flow, Nature 405 (2000) 53–55.
[55] E.M. Ekanem, S. Berg, S. De, A. Fadili, T. Bultreys, M. Rücker, J. Southwick, J. Crawshaw, P.F. Luckham, Signature of elastic turbulence of viscoelastic fluid flow in a single pore throat, Phys. Rev. E 101 (2020) 042605.
[56] C.A. Browne, A. Shih, S.S. Datta, Bistability in the unstable flow of polymer solutions through pore constriction arrays, J. Fluid Mech. 890 (A2) (2020).
[57] N. Zamani, I. Bondino, R. Kaufmann, A. Skauge, Computation of polymer in-situ rheology using direct numerical simulation, J. Petrol. Sci. Eng. 159 (2017) 92–102.
[58] T.W. van den Ende, Extensional viscosity aspects of HPAM in porous flow: An experimental and numerical study, Master thesis, TU Delft (2015).
[59] F. J. Galindo-Rosales, F. J. Rubio-Hernández, F. J., A. Sevilla, A., An apparent viscosity function for shear thickening fluids, Journal of Non-Newtonian Fluid Mechanics, 166(2011), 321–325.
[60] T. Shende, V.J. Niasar, M. Babaei, An empirical equation for shear viscosity of shear thickening fluids, J. Mol. Liq. 325 (2021) 115220.